Dynamics in near-threshold J/ψ photoproduction

D. Winney,[1,2,*] C. Fernández-Ramírez,[3,4,†] A. Pilloni,[5,6,‡] A. N. Hiller Blin,[7,8] M. Albaladejo,[9] Ł. Bibrzycki,[10] N. Hammoud,[11] J. Liao,[12,13] V. Mathieu,[14,15] G. Montaña,[16] R. J. Perry,[14] V. Shastry,[12,13,17] W. A. Smith,[12,13] and A. P. Szczepaniak[12,13,16]

(Joint Physics Analysis Center)

[1]*Guangdong Provincial Key Laboratory of Nuclear Science, Institute of Quantum Matter, South China Normal University, Guangzhou 510006, China*
[2]*Guangdong-Hong Kong Joint Laboratory of Quantum Matter, Southern Nuclear Science Computing Center, South China Normal University, Guangzhou 510006, China*
[3]*Departamento de Física Interdisciplinar, Universidad Nacional de Educación a Distancia (UNED), Madrid E-28040, Spain*
[4]*Instituto de Ciencias Nucleares, Universidad Nacional Autónoma de México, Ciudad de México 04510, Mexico*
[5]*Dipartimento di Scienze Matematiche e Informatiche, Scienze Fisiche e Scienze della Terra, Università degli Studi di Messina, I-98166 Messina, Italy*
[6]*INFN Sezione di Catania, I-95123 Catania, Italy*
[7]*Institute for Theoretical Physics, Regensburg University, D-93040 Regensburg, Germany*
[8]*Institute for Theoretical Physics, Tübingen University, D-72076 Tübingen, Germany*
[9]*Instituto de Física Corpuscular (IFIC), Centro Mixto CSIC-Universidad de Valencia, E-46071 Valencia, Spain*
[10]*Faculty of Physics and Applied Computer Science, AGH University of Krakow, PL-30-059 Kraków, Poland*
[11]*Institute of Nuclear Physics, Polish Academy of Sciences, 31-342 Kraków, Poland*
[12]*Center for Exploration of Energy and Matter, Indiana University, Bloomington, Indiana 47403, USA*
[13]*Department of Physics, Indiana University, Bloomington, Indiana 47405, USA*
[14]*Departament de Física Quàntica i Astrofísica and Institut de Ciències del Cosmos, Universitat de Barcelona, Barcelona E-08028, Spain*
[15]*Departamento de Física Teórica, Universidad Complutense de Madrid and IPARCOS, E-28040 Madrid, Spain*
[16]*Theory Center, Thomas Jefferson National Accelerator Facility, Newport News, Virginia 23606, USA*
[17]*Institute of Physics, Jan Kochanowski University, PL-25-406 Kielce, Poland*

(Received 10 May 2023; accepted 14 August 2023; published 13 September 2023)

The study of J/ψ photoproduction at low energies has consequences for the understanding of multiple aspects of nonperturbative QCD, ranging from mechanical properties of the proton to the binding inside nuclei and the existence of hidden-charm pentaquarks. Factorization of the photon-$c\bar{c}$ and nucleon dynamics or vector meson dominance are often invoked to justify these studies. Alternatively, open-charm intermediate states have been proposed as the dominant mechanism underlying J/ψ photoproduction. As the latter violates this factorization, it is important to estimate the relevance of such contributions. We analyze the latest differential and integrated photoproduction cross sections from the GlueX and $J/\psi - 007$ experiments. We show that the data can be adequately described by a small number of partial waves, which we parametrize with generic models enforcing low-energy unitarity. The results suggest a non-negligible contribution from open-charm intermediate states. Furthermore, most of the models present an elastic scattering length incompatible with previous extractions based on vector meson dominance and thus call into question its applicability to heavy mesons. Our results indicate a wide array of physics possibilities that are compatible with present data and need to be disentangled.

DOI: 10.1103/PhysRevD.108.054018

*dwinney@scnu.edu.cn
†cesar@jlab.org
‡alessandro.pilloni@unime.it

I. INTRODUCTION

The photoproduction of charmonia near threshold has garnered substantial interest, as it may give insight into a broad range of physics phenomena. Since the charm quark mass is heavy, it has been argued that charm production is a hard process. This motivates interpreting the amplitude in terms of factorized subprocesses, i.e. a hard photon-$c\bar{c}$ conversion and a soft proton matrix element. The two subprocesses exchange dominantly gluons, as the exchange of charm is suppressed by the heavy quark mass, and the exchange of light quarks is OZI suppressed [1]. In this form, the photoproduction amplitude gives information about the internal structure of the proton and has been related to gluonic PDFs [2] or GPDs [3], from which one extracts the gravitational form factors [3–5], the trace anomaly contribution to the proton mass [6–9], and the mass radius [10–12].

Extracting the elastic $J/\psi p$ amplitude is a necessary intermediate step for the determination of these quantities in some of frameworks, which is commonly done assuming vector meson dominance (VMD) [13–16]. The elastic scattering process is also interesting *per se*, as the small size of the $c\bar{c}$ pair compared to the nucleon suggests that the elastic scattering is driven by gluonic Van der Waals forces and can be described using the QCD multipole expansion [17–19]. Close to threshold, where the relative momentum between proton and J/ψ is small, the interaction is expected to be attractive and speculated to be strong enough to bind J/ψ to nucleons or even nuclei [20,21]. The J/ψ-nucleon total cross section is also of interest for heavy ion collisions, as final states with charmonia are a potential smoking gun for quark-gluon plasma [22–24].

The discovery of hidden-charm pentaquarks in the $J/\psi p$ spectrum at LHCb [25–27] has generated much interest in photoproduction searches, both theoretically [28–33] and experimentally [34–38]. Many theoretical studies highlight the role of open-charm channels in the formation of pentaquark signals [39–42], which suggest these contributions may also be relevant in near-threshold photoproduction [43] and potentially break factorization between hard charmonium production in the "top" vertex and the soft nucleon recoil in the "bottom" vertex.

Here we aim to address these questions by considering the photoproduction amplitude in a generic form, minimizing the model dependence and determining physical amplitude parameters solely from data. We describe data using a small number of s-channel partial waves (PWs), which we parametrize to satisfy unitarity constraints. This allows us to study the relevance of intermediate open-charm channels and test the VMD hypothesis. This approach is also general enough that resonance poles can emerge if data require them, allowing us to search for pentaquark states in the near-threshold region.

We consider the most recent data on total and differential cross sections from Jefferson Lab, in particular from GlueX [44] and the $J/\psi - 007$ experiment in Hall C [45]. The interplay between the different production mechanisms is subtle, and these new data offer the possibility to discern the dynamics with more detail.

The rest of the paper is organized as follows. In Sec. II, we review the unitary formalism to describe J/ψ production based on the near-threshold expansion. We consider four models of increasing complexity that offer different dynamical pictures and allow us to gauge systematic uncertainties. In Sec. III, we describe fits to the data and discuss implications for the nature of the underlying interactions. The four models describe the data with similar quality, and in some cases we find potentially large violations of factorization and VMD. Finally, in Sec. IV we summarize our results and discuss future experimental measurements needed to confirm these findings.

II. AMPLITUDE PARAMETRIZATION

We consider the process $\gamma p \to J/\psi p$ in the region from threshold ($E_\gamma \simeq 8.2$ GeV) to 12 GeV. The reaction amplitude depends on the standard Mandelstam variables s and t, i.e., the square of the center-of-mass energy and momentum transfer, respectively. In general, the amplitude also depends on the helicities of all four particles, but in the absence of polarization information the angular behavior can only be associated with the orbital motion determined by the angular momentum ℓ, and there is little point in considering spin degrees of freedom at this stage. We thus approximate the four particles as spinless and write the unpolarized cross section in the usual form,

$$\frac{d\sigma}{dt} = \frac{1}{16\pi(s - m_p^2)^2}|F(s,t)|^2, \tag{1}$$

and expand the scattering amplitude in terms of its s-channel PWs,

$$F(s,t) = \sum_\ell (2\ell + 1) P_\ell(\cos\theta) F_\ell(s), \tag{2}$$

where $\cos\theta \equiv \cos\theta(s,t)$ is the s-channel scattering angle. This expansion is particularly suitable to describe the region near threshold, where the infinite sum of partial waves is restricted by the angular momentum barrier factor, and is therefore expected to be saturated by a small number of terms. Furthermore, unitarity can be used to relate the imaginary part of the photoproduction amplitude to the hadronic final state interactions. In practice, unitarity is imposed effectively by considering only the most relevant two-body intermediate states. Thus, we write

$$\mathrm{Im}F_\ell(s) = F_\ell(s)\rho(s)T_\ell^\dagger(s), \tag{3a}$$

$$\mathrm{Im}T_\ell(s) = T_\ell(s)\rho(s)T_\ell^\dagger(s), \tag{3b}$$

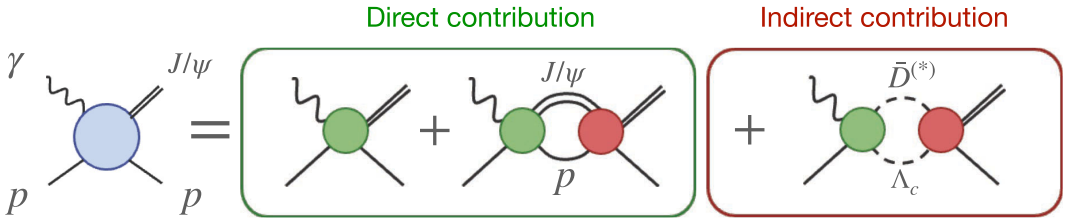

FIG. 1. Diagrammatic representation of the amplitudes in Eqs. (4) and (9). Each PW amplitude $F_\ell^{\psi p}$ (blue) receives contributions from a (short-range) production coupling f_ℓ (green) as well as terms proportional to the loop function G (Chew-Mandelstam phase space) and hadronic rescattering amplitude T_ℓ (red). The latter is summed over all intermediate channels that contribute.

where ρ is the two-body phase space of the intermediate state. When considering coupled channels, Eq. (3) represent matrix equations, with the matrix elements $F_\ell^i(s)$ and $T_\ell^{ij}(s)$ corresponding to the photoproduction amplitude of the ith final state and the $i \to j$ hadronic scattering amplitude, respectively. Although the $\bar{D}^{(*)}\Sigma_c^{(*)}$ channels have been proposed as relevant to the formation of hidden-charm pentaquarks [39–42], recent GlueX data show no obvious structures at the corresponding thresholds. Instead, a dip at $E_\gamma \simeq 9$ GeV is observed with an estimated significance of 2.6σ,[1] and thus we rather consider the effect of the $\bar{D}^{(*)}\Lambda_c$ channels, whose thresholds are located at $E_\gamma \simeq 8.7$ and 9.4 GeV, respectively, as suggested in Ref [43]. Since the data are available only for the $\gamma p \to J/\psi p$ process, and not for open-charm final states, their effects enter only indirectly through rescattering. In order to limit the number of free parameters, coupled channels are implemented in the S wave only, as threshold cusps are suppressed in higher waves, making it harder to disentangle the individual contributions of the various channels.

A solution of Eq. (3) is given by

$$F_\ell(s) = f_\ell(1 + GT_\ell) = f_\ell(1 - GK_\ell)^{-1}, \tag{4a}$$

$$T_\ell(s) = K_\ell(1 - GK_\ell)^{-1}, \tag{4b}$$

where the constraint of unitarity is satisfied as long as the K matrix K_ℓ and the production vector f_ℓ are real in the physical region. The relation between amplitudes in Eq. (4) is shown diagrammatically in Fig. 1. We set the Chew-Mandelstam phase space $G = \delta^{ij}G_i$ to satisfy $\mathrm{Im}G_i = \rho_i = q_i/8\pi\sqrt{s}$ and $G_i(s_i) = 0$ at the threshold of the ith intermediate state, $s_i = (m_{1i} + m_{2i})^2$ [46],

$$\begin{aligned} G_i &= \frac{s - s_i}{\pi}\int_{s_i}^{\infty} ds' \frac{\rho_i(s')}{(s' - s_i)(s' - s)} \\ &= -\frac{1}{\pi}\left[\rho_i \log\left(\frac{\xi_i + \rho_i}{\xi_i - \rho_i}\right) - \xi_i \frac{m_{2i} - m_{1i}}{m_{2i} + m_{1i}} \log\frac{m_{2i}}{m_{1i}}\right]. \end{aligned} \tag{5}$$

Here $q_i = \lambda^{1/2}(s, m_{1i}^2, m_{2i}^2)/2\sqrt{s}$ is the intermediate state 3-momentum and $\xi_i \equiv (1 - s_i/s)/16\pi$. For the (coupled-channel) S wave, we parametrize the production vector as a constant, while keeping terms up to $O(q_i^2)$ in the low-energy expansion of the K matrix,

$$f_S^i = n_S^i \quad \text{and} \quad K_S^{ij} = \alpha_S^{ij} + \beta_S^i q_i^2 \delta_{ij}, \tag{6}$$

with $\alpha_S^{ij} = \alpha_S^{ji}$ due to time reversal invariance. We found that adding more terms to the momentum expansion does not improve the quality of the fits. For waves with $\ell \geq 1$, we consider only the single $J/\psi p$ channel and therefore drop the channel indices. In this case, both the production vector and the K matrix are parametrized as constants, n_l and α_l, respectively, multiplied by the appropriate barrier factors,

$$f_\ell = (pq)^\ell n_\ell \quad \text{and} \quad K_\ell = q^{2\ell}\alpha_\ell. \tag{7}$$

Here $p = (s - m_p^2)/2\sqrt{s}$ is the incoming 3-momentum and $q \equiv q_{\psi p}$, as defined before.

In order to assess whether the current data can constrain the role of coupled channels, we consider three parametrizations of the S-wave amplitude:

(1) Single channel (1C): Only interactions involving the $J/\psi p$ are included.
(2) Two channels (2C): We include contributions from an intermediate $\bar{D}^*\Lambda_c$ channel.[2]
(3) Three channels (3C): We include both $\bar{D}^{(*)}\Lambda_c$ channels. In this case, we find two classes of solutions, which we discuss separately below.

Here the 1C parametrization is favored by the factorization picture of J/ψ photoproduction, as charm exchanges are suppressed by the heavy quark mass and the amplitude can be decomposed into a top vertex involving the photon interaction with a $c\bar{c}$ pair and a bottom vertex that depends on proton structure. Furthermore, it has been argued that near threshold the process is dominated by at most spin-2 exchanges in the t channel [8]. This allows one to relate the $J/\psi p$ photoproduction amplitude to the gluonic component of the nucleon energy-momentum tensor. Fixed spin

[1]The significance is only 1.4σ when considering the probability of any two adjacent points having a similar significance.

[2]The amplitude involving only the $J/\psi p$ and $\bar{D}\Lambda_c$ channels was also considered, but found to not be significant.

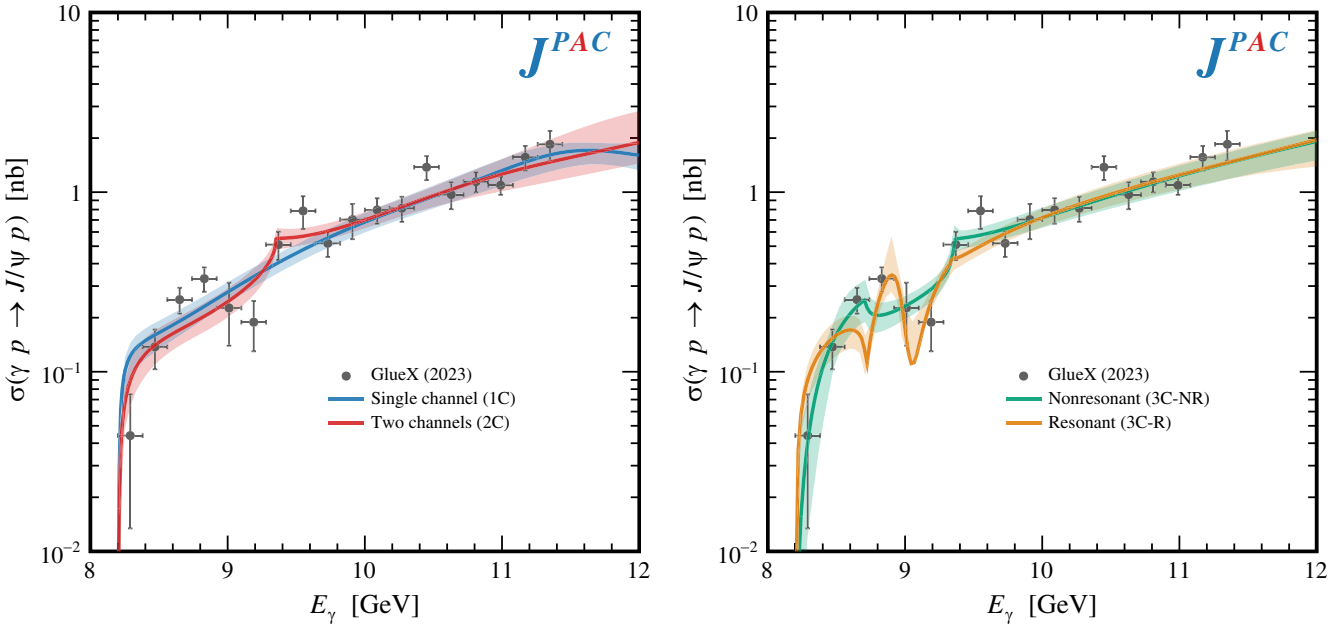

FIG. 2. Fit results for the integrated cross section of all four models compared to GlueX data from [44]. Bands correspond to 1σ uncertainties from bootstrap analysis.

t-channel exchanges lead to an analytical dependence on s and thus are not compatible with threshold cusps. The 1C case will be used at the base model with respect to which we evaluate the significance of extra thresholds.

Reference [43] estimates that the production rates of open-charm systems are much larger than hidden charm, and thus the coupling to intermediate open-charm states dominates the process of interest. This is representative of the 3C model, in particular, if the production parameters for the $J/\psi p$ system are small relative to those describing the open-charm channels. We consider the 2C model as an intermediate case between these two parametrizations, in which minimal freedom has been added to the 1C case to try to accommodate the apparent features of the total cross section.

In order to have a comparable number of free parameters in three parametrizations of the S wave, we consider both terms in the K matrix (i.e., α_S^{ij} and β_S^i) in the 1C and 2C cases, while the 3C parametrization keeps only the constant term in all channels. We find an adequate description of the angular dependence when truncating to $\ell_{\max} = 3$ in all cases.

Even if no explicit K-matrix pole is included, the amplitude in Eq. (4) can produce poles in the complex energy plane in all three parametrizations. If the pole appears sufficiently close to the physical region, it can be interpreted as a signal of a hidden-charm pentaquark.

III. RESULTS AND DISCUSSION

We analyze all of the recent Jefferson Lab (JLab) data from the GlueX [44] and $J/\psi - 007$ [45] experiments. This covers both the integrated cross section for the photon energies $E_\gamma = 8.2$–11.4 GeV and differential cross section reported in 15 energy bins. The differential cross section measurements of GlueX cover the entire physical t range. In total, we have 142 data points that we fit with each model described in Sec. II. We fit differential data at the reported $\langle t \rangle$ and $\langle E_\gamma \rangle$ values, which are averaged over the bin. Fits are performed by minimizing the standard χ^2 function with the experimental statistical and (uncorrelated) systematic uncertainties added in quadrature. We ignore correlations between integrated and differential cross sections. We note that the datasets from the two experiments have different normalization uncertainties ($\simeq$20% for GlueX and $\simeq$4% for $J/\psi - 007$). The fits are conducted under the assumption that the two datasets are consistent, and the correlated normalization errors are later included in the error analysis. The fit parameters were all initialized randomly and fits were repeated to sufficiently probe the parameter space. The resulting parameters for the best fits are summarized in the Appendix. For the 3C parametrization, we find two qualitatively different fit results with similar χ^2: one with a pole near the real axis, which we label 3C-R (resonant), and one without a nearby pole, which we label 3C-NR (nonresonant).

We determined uncertainties using a bootstrap approach [47], taking into account the statistical, systematic, and normalization uncertainties by assuming they are normally distributed. Further discussion of the propagation of uncertainties can be found in the Appendix. The resulting cross sections and associated uncertainties are shown in Figs. 2–4.

The simplest parametrization considered is the 1C scenario, which exhibits a smooth energy behavior,

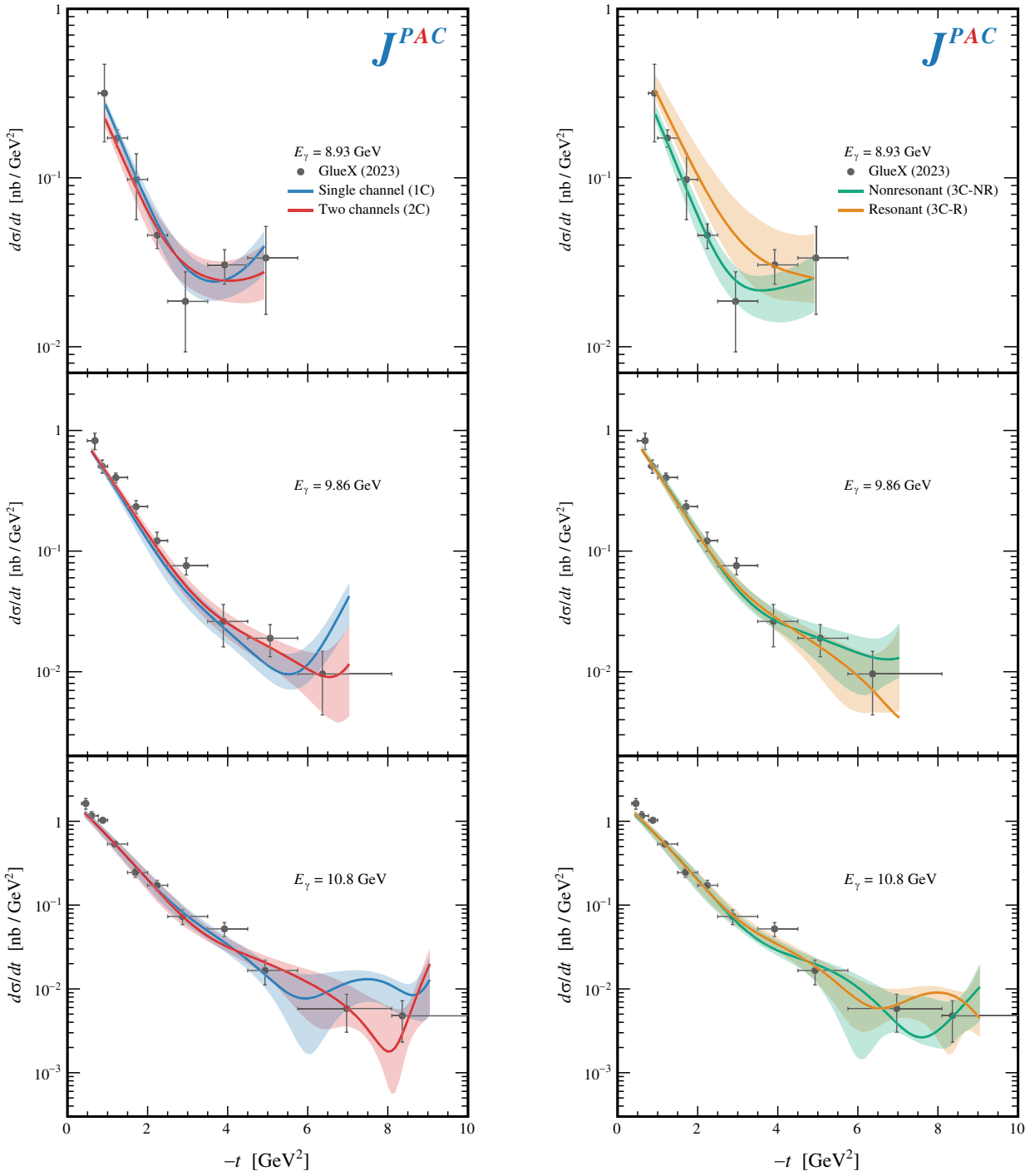

FIG. 3. Fit results for the differential cross section of all four models compared to GlueX data from [44]. The bands correspond to the 1σ uncertainties from the bootstrap analysis. The range of the data represents the entire physical t range at each fixed energy. The plotted theory curves are calculated at the average $\langle E_\gamma \rangle$ for each experimental energy bin.

since it contains no other channels that can give rise to threshold cusps. In the integrated cross section, the data points at the dip lie at least 2σ away from the fit curve, consistent with significance estimations in Ref. [44].

Extensions of the K matrix in Eqs. (6) and (7) were considered to study the systematics of the 1C results. Additional $O(q^4)$ and $O(q^2)$ terms were added to the S and P waves, respectively, but yielded no significant improvement over the original fit. Higher waves beyond $\ell = 3$ were

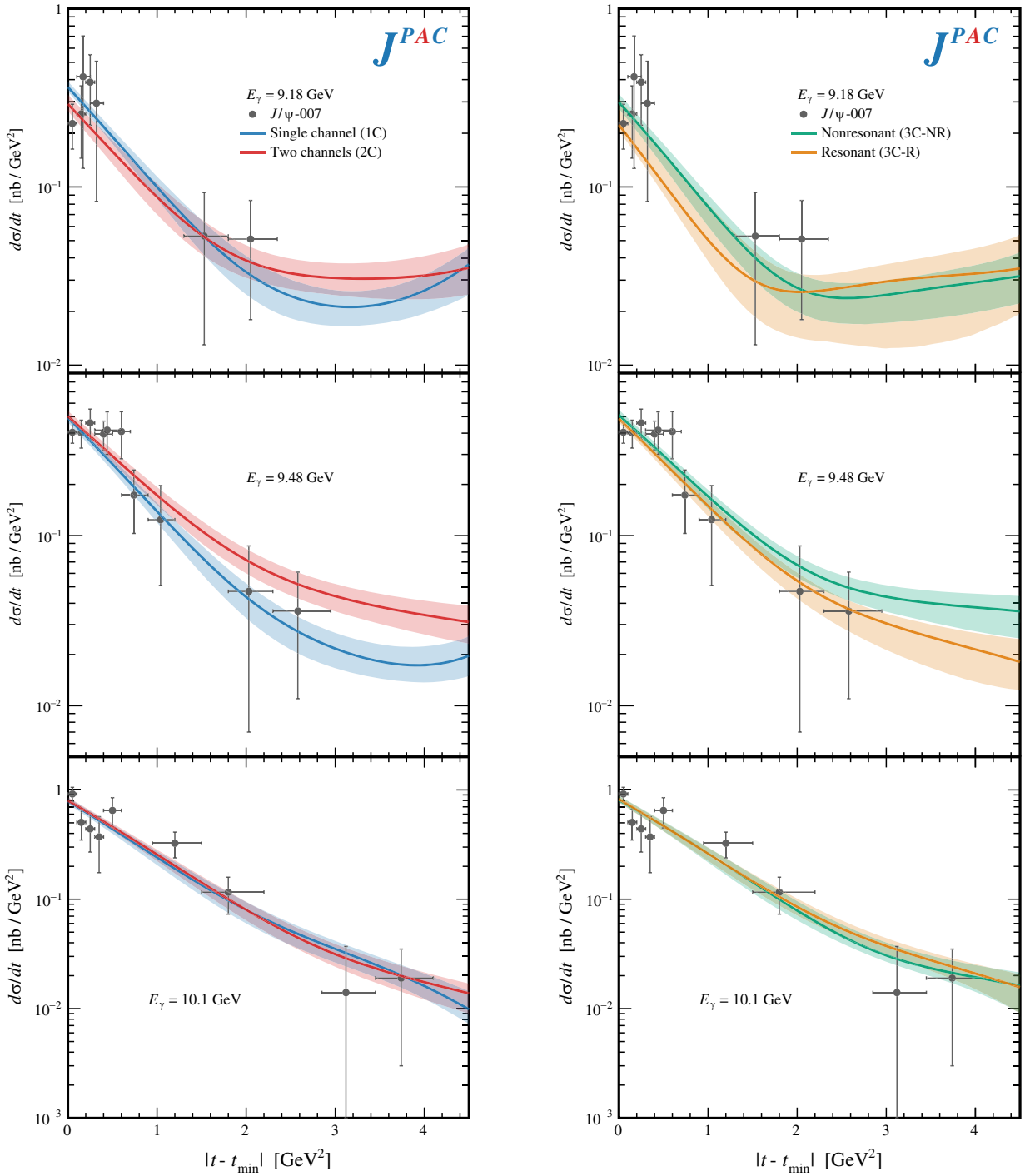

FIG. 4. Fit results for the differential cross section for all four models compared to $J/\psi - 007$ data from [45]. Here we only show three characteristic example slices in between those shown in Fig. 3, but all data are included in the fits. The bands correspond to the 1σ uncertainties from the bootstrap analysis. The plotted theory curves are calculated at the average $\langle E_\gamma \rangle$ for each experimental energy bin.

also considered, but had little impact on the best fit values of the lower PWs.

Adding the $\bar{D}^*\Lambda_c$ channel in the 2C model leads to a clear threshold cusp around $E_\gamma \simeq 9.5$ GeV. This improves the fit quality with respect to the single channel case, but the significance is not high enough to definitively favor this result over the 1C curve. Repeating the same analysis considering the lighter $\bar{D}\Lambda_c$ channel instead does not constitute a significant improvement over the 1C fit, with best fit open-charm parameters found to be consistent with zero.

The curves with the most structure arise from the 3C model containing both open-charm thresholds. These fits

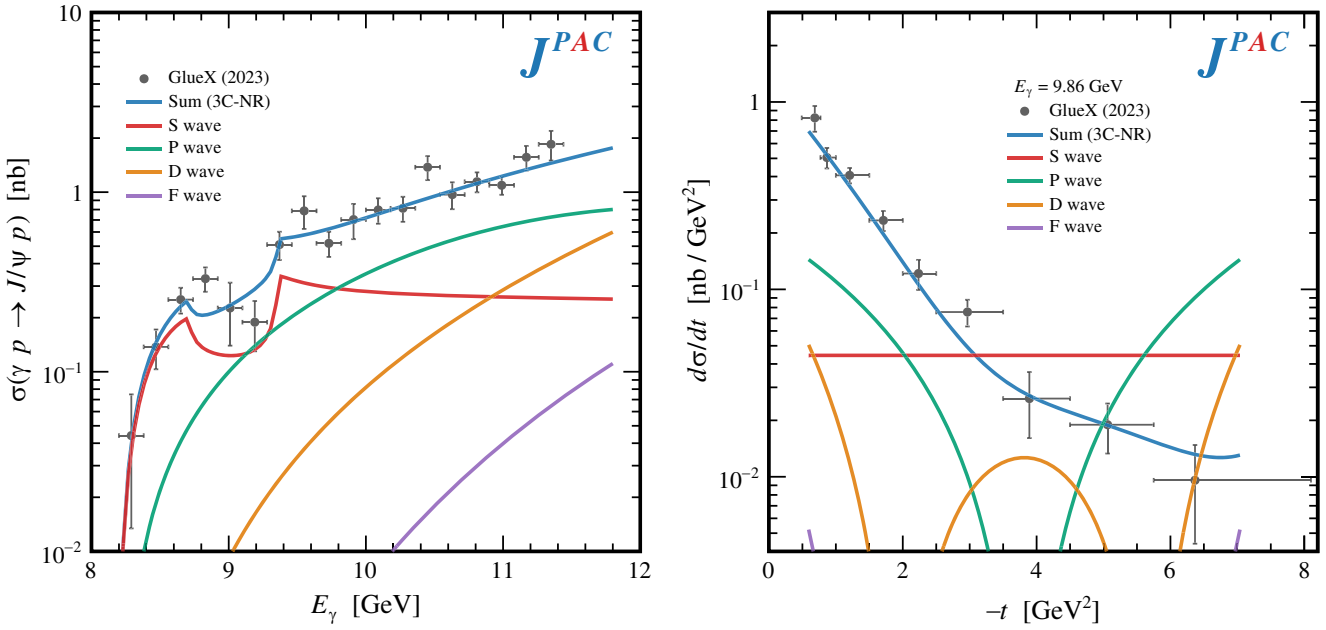

FIG. 5. Comparison of individual PW contributions to the cross sections from GlueX [44] using the 3C-NR best fit parameters. In the differential cross section, the Legendre polynomials interfere to give rise to the sharp t distribution reminiscent of the diffractive peak. A similar hierarchy of waves is seen in all fit results.

showcase dips similar to those apparent in the data, but differ in the precise line shape between the two open-charm thresholds, meaning comparison between these is sensitive to the details of the cusp-dip structure. We see the 3C-NR shape is reminiscent of predictions from the box diagram calculation in [43]. The other fit, labeled 3C-R, exhibits an even more pronounced line shape, which is due to the presence of a nearby pole singularity, the implications of which will be discussed in Sec. III F.

A. Momentum transfer distributions

Differential data near threshold have been proposed as a means to access the gluonic gravitational form factors and mass radius of the proton (see, e.g., [8,11,45] and references therein). The observed behavior in t poses interesting questions about the $J/\psi p$ interaction itself.

At high energies, the photoproduction of vector quarkonia has been extensively studied at HERA [48,49]. In this energy region, the process is diffractive and generally understood through gluonic exchanges, realized, e.g., as a Pomeron [50] or in a color-dipole model [51]. The differential distributions are characterized by their "diffractive peak" at forward t and exponential dropoff at high transferred momentum. Previous measurements of the differential cross section seem to observe the same behavior even at lower energies [34,52] and are confirmed by the newest GlueX measurement for $E_\gamma > 9$ GeV. At the lowest energy value $\langle E_\gamma \rangle = 8.9$ GeV, the last few bins at largest t seem to turn upward and have drawn attention as potential indications of u-channel exchanges or other s-channel contributions. However, since each PW series in the s, t, or u channel is a full representation of the amplitude, these contributions cannot be simply added, but the whole process has to be studied consistently from one perspective.

Explaining the apparent exponential behavior of the t distributions with the finite PW sum of Eq. (2) does not immediately seem natural. Each s-channel PW has polynomial angular (and therefore t) dependence, unlike commonly used dipole or exponential form factors, so one would naively expect that a large number of PWs are needed to describe data. Instead, we find a good description only considering terms with $\ell \leq 3$. The emergence of the sharp asymmetric t distribution is due to interference between the PW amplitudes, as waves with odd and even ℓ interfere constructively at forward angles and destructively at backward ones [i.e., through $P_\ell(\cos\theta = \pm 1) = (\pm 1)^\ell$]. Individual contributions to the cross sections are plotted in Fig. 5 for the 3C-NR case.

In order to more quantitatively explore the convergence of the PW series, we may examine the radius of interaction r that enters with the angular momentum barrier,

$$r^{2\ell} \equiv \lim_{s \to s_{\rm th}} \left| \frac{F_\ell(s)/(pq)^\ell}{F_S(s)} \right|, \tag{8}$$

where $s_{\rm th} = (m_\psi + m_p)^2$ is the photoproduction threshold. As long as $pqr^2 < 1$, we may expect any subsequent waves to be suppressed and the use of a finite number of PWs to be justified. Technically speaking, the interaction radius varies per PW, but we care about the typical value with

TABLE I. Summary of fit results. For each solution, we tabulate the number of parameters χ^2 and reduced χ^2. We also tabulate the 90% CL interval of each dynamical quantity described in the text (see the Appendix). In order, these are the ratio of production mechanisms defined in Eq. (10), the VMD ratio in Eq. (12) (extracted for both $\theta = 0$ and $t = 0$ prescriptions), and the elastic $J/\psi p$ scattering length in Eq. (13).

	1C	2C	3C-NR	3C-R
Parameters	9	13	15	15
χ^2	166	144	141	143
χ^2/d.o.f.	1.25	1.12	1.11	1.13
$\zeta_{\rm th}$	1	[0.56, 0.74]	[0.36, 0.63]	[0.03, 0.62]
$R_{\rm VMD}(\theta = 0)$	$[0.45, 0.73] \times 10^{-2}$	$[0.39, 1.62] \times 10^{-2}$	$[0.03, 1.74] \times 10^{-2}$	$[1.4 \times 10^{-2}, 0.58]$
$R_{\rm VMD}(t = 0)$	$[1.3, 2.0] \times 10^{-2}$	$[1.3, 5.1] \times 10^{-2}$	$[0.08, 8.9] \times 10^{-2}$	$[5.4 \times 10^{-2}, 1.8]$
$a_{\psi p}$ (fm)	[0.56, 1.00]	[0.11, 0.79]	$[-2.77, 0.35]$	$[-0.04, 0.19]$

which to characterize the rate of convergence. For all fit results, the radius is found to be $r \simeq 0.1$ fm. Since the PWs may also vary independently as a function of s, we additionally consider the limit Eq. (8) taken to the end point energy of the data, $E_\gamma \simeq 12$ GeV. We find the energy dependence is extremely mild and we maintain the same average r value. Thus, extrapolating this to the transition energy satisfying $pqr^2 = 1$, we may expect the description in terms of s-channel PWs to hold up to about $E_\gamma \sim 14$ GeV. At energies beyond this point, there is no suppression of higher waves and the infinite series must be resummed, characteristic of the Regge regime.

The fact that all amplitude models reproduce the differential data accurately seems to suggest that the shape of the momentum transfer distribution alone does not discriminate details of the individual PWs with the current precision. Furthermore, Fig. 3 demonstrates that all models, resonant and nonresonant, reproduce the apparent upward behavior of the lowest energy slice of the GlueX measurement. This suggests the enhancement at backward t very close to threshold is not necessarily indicative of s-channel resonances.

B. Production mechanisms

As previously mentioned, establishing that charmonium photoproduction near threshold is due to short-range fluctuations in the photon beam is needed in order to be able to use this reaction to extract the proton tensor charge. If the contribution from charm exchange is found to be sizable, this process may be a low-energy probe of the intrinsic charm component of the nucleon wave function [53,54], whose extraction from inclusive measurements at higher energies has recently been studied [55,56].

The formalism in Sec. II allows us to clearly identify production quantities for each channel individually, and thus we can test the factorization hypotheses by assessing the strength of open-charm contributions based on available data. The coupled-channel S-wave amplitude in Eq. (4) can be explicitly written as

$$F_S^{\psi p}(s) = \overbrace{n_S^{\psi p}(1 + G^{\psi p} T_S^{\psi p,\psi p})}^{F^{\psi p}_{\rm direct}(s)} + \overbrace{(n_S^{\bar{D}\Lambda_c} G^{\bar{D}\Lambda_c} T_S^{\bar{D}\Lambda_c,\psi p} + n_S^{\bar{D}^*\Lambda_c} G^{\bar{D}^*\Lambda_c} T_S^{\bar{D}^*\Lambda_c,\psi p})}^{F^{\psi p}_{\rm indirect}(s)}, \tag{9}$$

where we identify terms corresponding to the two production mechanisms as depicted diagrammatically in Fig. 1. The "direct" amplitude is composed of contributions in which the initial γp state couples directly to $J/\psi p$, while in the "indirect" contributions γp produces an intermediate open-charm pair first, before rescattering into the final $J/\psi p$.

The relative strengths of these two terms allow us to gauge which photoproduction mode is more relevant in the region of interest. To more easily quantify this, we define the ratio

$$\zeta_{\rm th} = \frac{|F^{\psi p}_{\rm direct}(s_{\rm th})|}{|F^{\psi p}_{\rm direct}(s_{\rm th})| + |F^{\psi p}_{\rm indirect}(s_{\rm th})|}. \tag{10}$$

Clearly, the 1C case has $\zeta_{\rm th} = 1$, while $\zeta_{\rm th} \simeq 0$ would indicate the J/ψ is almost entirely produced through intermediate open charm. Since the latter requires flavor exchange between the top and bottom vertices, it would explicitly break factorization.

Examining the line shapes in Fig. 2, one might naively assume that the cusps are a small contribution to an otherwise smooth background from the direct reaction. However, since the various terms are added at the amplitude level, this might not necessarily be the case. We tabulate the extracted values of $\zeta_{\rm th}$ in Table I, which indicates the indirect contributions play a non-negligible role. The direct amplitude contributes only $\zeta_{\rm th} \lesssim 75\%$ at 90% confidence level (CL) in all coupled-channel parametrizations, with the 3C-R result even compatible with $\zeta_{\rm th} = 0$. Clearly, deviations of $\zeta_{\rm th}$ from unity are due to the presence of the 9 GeV dip in the data, which can only be captured with a sizable

coupling to open charm. Thus, if future data confirm the dip, the implications for factorization and the extraction of proton observables will need to be addressed.

C. Vector meson dominance

The VMD assumption has been used extensively in the analysis of photon-hadron interactions and, in particular, in the extraction of proton observables [2,57,58]. This posits that the photoproduction interaction can be modeled by replacing the incident photon by the hadron spectral function, generally modeled as a sum of vector meson propagators, and multiplying each term by a known constant related to the vector meson electromagnetic width. Although it has been argued that, in particular, for heavy quarkonia, the sum over higher vectors should be retained (so-called generalized VMD [59]), most of the literature about charmonium photoproduction at threshold restricts the sum to the lightest J/ψ, as it allows one to relate photoproduction to the elastic scattering amplitude,

$$F^{\psi p}(s,x) = g_{\gamma\psi} T^{\psi p,\psi p}(s,x). \tag{11}$$

Here $x = t$ or θ depending on whether this relation is considered at fixed momentum transferred or scattering angle, i.e., through two different $t = t(s,\cos\theta)$ for the photoproduction and elastic reactions.[3] The proportionality constant $g_{\gamma\psi}$ represents the $\gamma \to c\bar{c}$ transition strength and is related to the J/ψ decay constant $g_{\gamma\psi} = e f_\psi / m_\psi \simeq 0.0273$ extracted from the J/ψ electronic width. In quark models, the latter is related to the quarkonium wave function at the origin [60,61]. The core assumption is that the proton acts as a spectator when the J/ψ is formed and thus the energy dependence of production and elastic amplitudes is the same.

In contrast, the structure of the photoproduction amplitude dictated by near-threshold unitarity in Eq. (4) illustrates that photoproduction and elastic scattering amplitudes are not necessarily proportional. While it may be the case that VMD still holds, our analysis does not rely on it, and the relation between production and elastic amplitudes is determined solely by data. This means we may directly compare the photoproduction and elastic amplitudes and gauge if VMD is justified in the near-threshold region. We quantify this test by defining the ratio,

$$R_{\rm VMD}(x) = \left| \frac{F^{\psi p}(s_{\rm th},x)/g_{\gamma\psi}}{T^{\psi p,\psi p}(s_{\rm th},x)} \right|, \tag{12}$$

where the numerator would be the elastic amplitude calculated assuming Eq. (11), while the denominator is the one extracted directly from Eq. (4). We fix $s = s_{\rm th}$ for concreteness and use the reference value of $g_{\gamma\psi}$ quoted above. Since Eq. (2) is entirely analytic, we may compute $R_{\rm VMD}$ either at fixed $\theta = 0$,[4] or at the unphysical point $t = 0$—e.g., as done in [14,16] or in [2,13,57], respectively. If VMD is an accurate approximation of the production amplitude, we should expect $R_{\rm VMD} \simeq O(1)$. Instead, the results in Table I suggest that VMD underestimates the amplitude by 2 orders of magnitude regardless of evaluation in almost all the fit results. The only exception is the 3C-R model, which has the largest uncertainties.

If these results were to be confirmed, the applicability of VMD in the heavy quarkonium sector would be severely questioned, affecting the widespread application of VMD in theoretical studies. For example, the current upper limits on hidden-charm pentaquark branching fractions in photoproduction are based on VMD models and sit at the sub-1% level [32,34]. If VMD is so drastically violated, pentaquarks may still have sizable branching ratios, $\mathcal{B}(P_c \to J/\psi p) \simeq O(10\%)$, but a much smaller photocoupling than expected (compatible with estimations in [62]), which makes them more difficult to observe in photoproduction.

D. $J/\psi p$ scattering length

One immediate consequence of a failure of VMD is its effect on the extraction of the elastic scattering length from photoproduction data. This is of fundamental importance, as it may enter the proton mass decomposition [57], provides motivation for color transparency [63], and suggests the possible emergence of bound states [20,64,65].

In our normalization, the scattering length $a_{\psi p}$, is related to the S-wave elastic scattering amplitude close to threshold by

$$T_S^{\psi p,\psi p} = \frac{8\pi\sqrt{s_{\rm th}}}{-a_{\psi p}^{-1} - iq} + O(q^2). \tag{13}$$

Using VMD, i.e., assuming Eq. (11), this relation leads to

$$\text{VMD:}\ F^{\psi p}(s_{\rm th},x) = -8\pi\sqrt{s_{\rm th}} g_{\gamma\psi} a_{\psi p}. \tag{14}$$

This means that the square of the scattering length is assumed to be directly related to the normalization of the photoproduction differential cross section at threshold (extrapolated at $t = 0$) or the normalization of the total cross section divided by the phase space (for $\theta = 0$). In this way, a small photoproduction cross section will directly translate into a small scattering length, which does not need to be the case. In our framework, unitarity gives a relation at the PW level, which means that the photoproduction is related to the scattering one at fixed θ. In the simplest 1C case, the equivalent expression using Eqs. (3) and (13) yields

$$\text{1C:}\ F^{\psi p}(s \to s_{\rm th},\theta) = n_S^{\psi p}(1 - iq a_{\psi p}) + O(q^2), \tag{15}$$

[3]For a more detailed discussion regarding these two forms of Eq. (11), see Ref. [15] and references therein.

[4]The same relation holds for any fixed value of θ; we select $\theta = 0$ for aesthetic reasons.

where one sees the scattering length drops out of the normalization and can only be extracted from the energy dependence. This relation gets even more complicated for coupled channels, as the indirect contributions of Eq. (9) will enter the equation, but the conclusion is the same: the normalization of photoproduction and the elastic scattering length are, in general, independent.

Scattering lengths $O(1\ \mathrm{fm})$ would indicate a typical hadronic interaction between the charmonium and nucleon and are consistent with the range of theoretical predictions based on the QCD multipole expansion [66,67], gluonic Van der Waals forces [19], QCD sum rules [68], and some lattice QCD extractions [69,70]. Previous VMD-based extractions from data have yielded scattering lengths up to 3 orders of magnitude smaller [15], similar to expectations from effective field theories [43] and some lattice studies [71]. The smallness of the scattering length relative to the proton size has been argued to be related to the compact size of the $c\bar{c}$ pair, rendering it "transparent" to the proton.

The extracted values for all fits are reported in Table I. Fits 1C and 2C, which have the best constrained parameters, give scattering lengths of the order of a Fermi at 90% CL, in stark contrast to VMD-based extractions. The values obtained from the 3C models, on the other hand, are consistent with zero in both the resonant and nonresonant models. Interestingly, the 3C-NR interval reveals a propensity for larger, negative scattering lengths, while the 3C-R extracts $|a_{\psi p}| \lesssim 0.2$ fm at a 90% CL.

While there is a clear preference for larger values of the scattering length and severe violation of VMD, the poorly constrained 3C models do not allow definitive conclusions to be drawn. Further data on the dip region and direct measurements of open-charm photoproduction will better constrain the parameters of coupled-channel models and therefore resolve the size of the scattering length.

E. Total $J/\psi p$ cross section

Establishing a relation between charmonium photoproduction and elastic scattering is also of relevance for quantitative descriptions of the charmonium interaction and evolution within the many-body hadronic medium at the final stage of heavy ion collisions [22,72–75]. Phenomenological simulations of the charmonia suppression in these collisions, which have nontrivial implications as a signature of the quark-gluon plasma phase, would rely on accurate knowledge of such cross sections.

Since the charmonium scattering is not achievable experimentally, estimations for cross sections must be inferred indirectly. Until recently, the lack of data on charmonium production near threshold meant that the cross section at the low energies was poorly known. The existing estimates from near-threshold photoproduction data came from SLAC in the 1970s and used either VMD assumptions [52] or the A dependence considering various nuclear targets [76] to estimate the total cross section at a beam energy $E_\gamma \simeq 20$ GeV ($\sqrt{s} \simeq 6.2$ GeV). The values extracted using

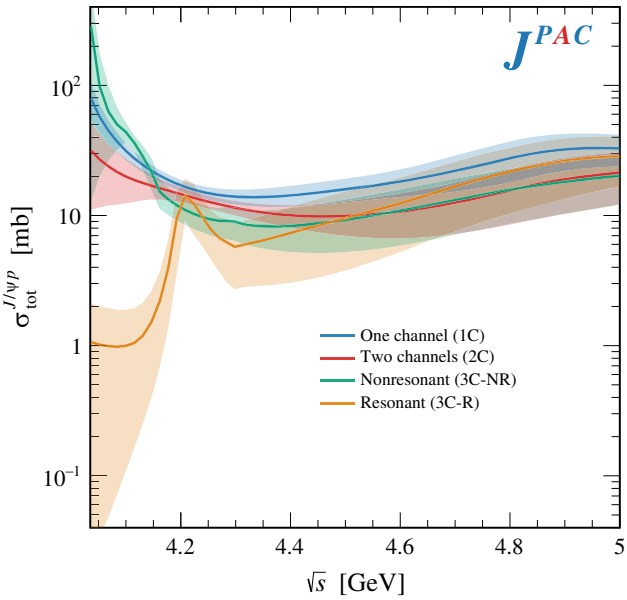

FIG. 6. Near-threshold total hadron cross section of the charmonium-nucleon system calculated for each of our fit results. Bands correspond to 1σ uncertainties calculated by bootstrap analysis. The pentaquark contribution is evident in the resonant case.

the different methods, ∼0.3 and ∼4 mb, respectively, revealed a large discrepancy between the extractions with VMD yielding a significantly smaller value (see also discussion in Ref. [77]).

Theoretical estimates for the total cross section, e.g., using color dipole models [78], constituent quark models [79,80], or meson exchange models [81–83], have also predicted a broad range of values for the cross section from fractions of a millibarn to upward of ∼10 mb near threshold.

Because our formalism has access to the elastic amplitude directly, we may consider the total $J/\psi p$ cross section from our fit results. Using the optical theorem, we calculate

$$\sigma_{\mathrm{tot}}^{\psi p} = \frac{1}{2q\sqrt{s}} \mathrm{Im} T^{\psi p,\psi p}(s, t=0), \tag{16}$$

which we plot for all fit cases in Fig. 6. At energies just above threshold, the overall size of the cross section is dominated by the S-wave scattering length. As demonstrated in Sec. III D, this is sensitive to the dynamics of the S wave and varies drastically depending on the parametrization used. Further, we notice the clear resonant peak that appears in the 3C-R model. At higher energies, the cross section is dominated by higher waves, where we see a closer overlap of values. At $\sqrt{s} = 5$ GeV, we find $\sigma_{\mathrm{tot}}^{\psi p} \gtrsim 8$ mb at a 90% CL in all amplitudes that include open-charm contributions, while the 1C case has $\gtrsim$20 mb.

These numbers are roughly compatible with the SLAC measurement not assuming VMD, although an explicit quantitative comparison is not possible with our near-threshold formalism, as the data are at energies beyond

the radius of convergence of the PW expansion (see Sec. III A).

F. Pentaquark searches

The parametrization of the K matrix is general enough that poles may still emerge if favored by the data. In particular, this allows for the possibility of pentaquark poles that feature non–Breit-Wigner line shapes due to complicated multichannel dynamics in the S wave.

For a given set of parameters, we may locate poles in Eq. (4) by searching for roots of $\det(1 - GK_\ell)$ in the complex energy plane for every Riemann sheet. Care must be taken in the analytic continuation of the amplitude, especially in coupled-channel parametrizations, to identify the relevant Riemann sheets and their proximity to the real axis [84].

No bound state poles are found in the energy region of interest in any PW for the 1C or 2C best fit results. Attempts to guide these parametrizations to a resonant minimum were done by first fitting only the GlueX total cross section as in [85]. Resulting fits featuring resonant poles were then used as the initial values to fits using the full dataset. Such fits were found to always produce either the quoted nonresonant best fit or a significantly worse local minimum.

The 3C-NR result presents S-wave poles located on Riemann sheets far away from the physical axis and thus unlikely associated with pentaquark candidates. On the other hand, the remaining 3C-R fit is found to contain three narrow S-wave poles, one of which is compatible with a pentaquark state. We stress that the uncertainties for the 3C fits are the largest and the precise locations of these poles cannot be determined when a detailed bootstrap analysis is performed. Because of this, we report pole positions for the best fit found without uncertainties and focus on the qualitative implications for the $\gamma p \to J/\psi p$ reaction.

Using the parameters for the 3C-R best fit, the most relevant pole has a mass of $M = 4211$ MeV and a width of $\Gamma = 48$ MeV, placing it between the $\bar{D}\Lambda_c$ and $\bar{D}^*\Lambda_c$ thresholds. In a common notation denoting the relative position to each of the three thresholds [84], this pole is located on Riemann sheet $(--+)$, which is the closest to the physical region. The pole position corresponds to a beam energy of $E_\gamma \sim 9$ GeV and coincides with the structure visible in Fig. 2. Besides this, two other poles are found on more remote sheets: one is a mirror pole of the above located on $(-++)$, with the same mass and width, and the other pole is located close to the real axis with $M = 4070$ MeV on $(+-+)$.

Again, with the present statistics, definitive conclusions regarding these poles cannot be drawn. Still, these results suggest the recent experimental measurements leave room for the appearance of poles in scenarios with strongly coupled higher channels. Specifically, it suggests the precise line shape in the dip region is diagnostic of the presence of pentaquarks whose identification may require a sophisticated analysis.

Apart from exciting implications for spectroscopy, the existence of bound states in this region would constitute an unambiguous violation of factorization.

IV. SUMMARY AND OUTLOOK

In this work, we analyzed the recent JLab J/ψ photoproduction data near threshold using generic low-energy parametrizations. Most of the literature regarding this reaction relies on specific underlying dynamics of the J/ψ-proton interaction, such as the factorization of the nucleon matrix elements. Since these works relate to fundamental properties of the proton, it is important to test the validity of these assumptions against available data. We have demonstrated that both integrated and differential cross sections can be described with a small number of partial waves, parametrized with customary low-energy expansions. We have incorporated the effects of nearby open-charm thresholds and extracted quantities that characterize the physics underlying the data. Our results highlight the wide array of physics that may be at play in this energy region.

We have presented four models of increasing complexity, which describe the current data with similar quality but represent different dynamical pictures. We have shown how to extract the elastic $J/\psi p$ amplitude from our models while respecting S-matrix constraints. Our analysis indicates that present statistics do not exclude severe violations of factorization and of the vector meson dominance that are usually assumed in the literature. This may affect the extraction of the elastic scattering length, total charmonium-nucleon cross section, and proton structure observables, as well as pentaquark searches.

It is thus crucially important to constrain model parameters with further measurements in order to disentangle the possible physics scenarios and their implications. In addition to higher statistics, especially to resolve the line shape around the 9 GeV dip, the measurement of open-charm photoproduction is needed to assess the role of coupled channels. A simultaneous analysis of the $\gamma p \to J/\psi p, \bar{D}^{(*)}\Lambda_c$ cross sections would provide a stringent constraint on coupled-channel dynamics. Based on the best fit parameters extracted here, we expect a large open-charm cross section $\gtrsim 10$ nb. Furthermore, studies of photoproduction off nuclear targets may give further constraints on the total J/ψ-nucleon cross section [86].

Polarization observables were previously proposed as an alternative means to search for pentaquarks [32]. This takes advantage of photoproduction facilities' unique capabilities for polarized beam-target setups in accessing helicity dependence. Measuring the J/ψ spin density matrix or spin asymmetries would give access to helicity couplings and may help further separate the mechanisms at play. Although not considered here, the formalism of Sec. II is readily extendable to allow an analysis that includes spin

degrees of freedom when such data become available. Our framework can also be applied to the analysis of other vector mesons, such as the analysis of Υ photoproduction data when it becomes available in the future.

The future of heavy meson photoproduction looks promising, with proposals for both upgrading existing experiments, including measurements in every hall of JLab [36,37,86,87], to further study the near-threshold region, as well as new electron-hadron facilities [88,89]. In addition, the proposed 24 GeV CEBAF upgrade [90,91] aims to extend the Jefferson Lab physics program to the charmonium sector. This will give the possibility of also studying higher charmonia in photoproduction [92,93], which may give key insight into the role of coupled channels and probe quarkonium wave function dependence to further understand the applicability of VMD in charmonium sectors.

All codes necessary to reproduce the results of this article are publicly available at [94].

ACKNOWLEDGMENTS

We thank S. Dobbs, K. Mizutani, and L. Pentchev for their comments and insight into the GlueX data. This work was supported by the U.S. Department of Energy Award No. DE-AC05-06OR23177, under which Jefferson Science Associates, LLC operates Jefferson Lab, and also by the U.S. Department of Energy Awards No. DE-FG02-87ER40365 and No. DE-FG02-92ER40735, by U.S. National Science Foundation Grant No. PHY-2209183, by the Spanish Ministerio de Ciencia e Innovación (MICINN) Grants No. PID2020–112777 GBI00, No. PID2019–106080 GB-C21, and No. PID2020–118758 GB-I00. D. W. is supported by National Natural Science Foundation of China Grant No. 12035007 and the NSFC and the Deutsche Forschungsgemeinschaft (DFG, German Research Foundation) through the funds provided to the Sino-German Collaborative Research Center TRR110 "Symmetries and the Emergence of Structure in QCD" (NSFC Grant No. 12070131001, DFG ProjectID 196253076-TRR 110). C. F. R. is supported by Spanish Ministerio de Educación y Formación Profesional under Grant No. BG20/00133. A. N. H. B. is supported by the DFG through the Research Unit FOR 2926 (Project No. 409651613). M. A. is supported by Generalitat Valenciana under Grant No. CIDEGENT/2020/002. N. H. is supported by a Polish research project with No. 2018/29/

TABLE II. Best fit results from χ^2 minimization for the four fit results considered. For the 3C model, we provide two fits of similar quality and different underlying dynamics. They are labeled 3C-(N)R for (non)resonant as described in the main text. All numbers are expressed in appropriate GeV units.

	1C	2C	3C-NR	3C-R
No. parameters	9	13	15	15
χ^2	166	144	141	143
χ^2/d.o.f.	1.25	1.12	1.11	1.13
$n_S^{\psi p}$	0.063	0.101	0.105	8.77×10^{-3}
$n_S^{\bar{D}\Lambda_c}$			−0.103	9.80
$n_S^{\bar{D}^*\Lambda_c}$		3.214	−0.089	−0.012
$\alpha_S^{\psi p,\psi p}$	−418.24	−219.68	−258.12	−86.75
$\alpha_S^{\psi p,\bar{D}\Lambda_c}$			168.24	−1.34
$\alpha_S^{\psi p,\bar{D}^*\Lambda_c}$		5.00	−132.60	−88.97
$\alpha_S^{\bar{D}\Lambda_c,\bar{D}\Lambda_c}$			−135.60	224.25
$\alpha_S^{\bar{D}\Lambda_c,\bar{D}^*\Lambda_c}$			235.48	0.081
$\alpha_S^{\bar{D}^*\Lambda_c,\bar{D}^*\Lambda_c}$		47.10	93.98	−294.93
$\beta_S^{\psi p,\psi p}$	320.76	−180.31		
$\beta_S^{\bar{D}^*\Lambda_c,\bar{D}^*\Lambda_c}$		−145.68		
n_P	18.3×10^{-3}	14.6×10^{-3}	16.1×10^{-3}	14.02×10^{-3}
α_P	−133.77	−44.00	−61.24	−87.80
n_D	3.08×10^{-3}	3.03×10^{-3}	3.63×10^{-3}	3.65×10^{-3}
α_D	−36.32	−2.34	−4.77	−16.55
n_F	0.81×10^{-3}	0.69×10^{-3}	0.52×10^{-3}	0.66×10^{-3}
α_F	−25.91	−6.01	3.14	−10.17

B/ST2/02576 (National Science Center). V. M. is supported by a Serra Húnter fellowship. V. S. acknowledges the support of the U.S. DOE ExoHad Topical Collaboration, Contract No. DE-SC0023598. This research was supported in part by Lilly Endowment, Inc., through its support for the Indiana University Pervasive Technology Institute. We acknowledge the computational resources and assistance provided by the Centro de Computación de Alto Rendimiento CCAR-UNED. This work contributes to the aims of the U.S. Department of Energy ExoHad Topical Collaboration, contract DE-SC0023598.

APPENDIX: BEST FIT PARAMETERS AND UNCERTAINTY ESTIMATION

In Table II we provide the best fit results from the χ^2 minimization of the four models considered. These parameters are highly correlated and, because their absolute size is not of interest *per se*, we do not show uncertainties. Instead, for each fit case, we compute 68% CL uncertainties for the curves of both integrated and differential cross sections and 90% CL for the extracted dynamical quantities reported in Table I. Using a bootstrap analysis [47], all sources of experimental uncertainties, i.e., statistical, uncorrelated systematics, and correlated systematics are propagated to each quantity of interest. To compute the confidence intervals, we perform 10^4 bootstrap fits to obtain the distribution for each quantity.

Because this minimization is ill posed, it is possible for some bootstrap fits to end in local minima that are quite far away from the best fit. Such outliers are clearly separated from the rest of the distribution and highly affect the extracted mean and standard deviation unrealistically. In order to handle this, for the error estimations in Table I, we use an iterative process to prune outliers and achieve a more realistic error estimation. For a given distribution, we compute the mean and standard deviation and remove any values 4σ away from the mean. This step is repeated until all values in the remaining distribution lie within 4σ.

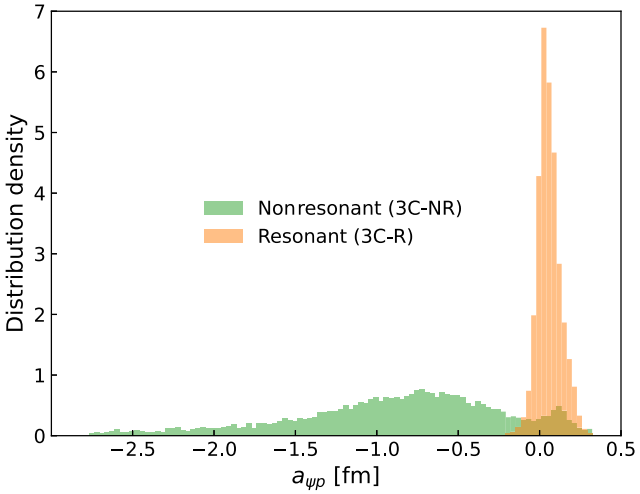

FIG. 7. Distribution of the $a_{\psi p}$ values obtained from the bootstrap and used to compute their uncertainties in Table I for the 3C-R and 3C-NR. The area of each distribution is normalized to unity. A secondary peak is clearly visible near $a_{\psi p} \simeq 0.1$ fm in the 3C-NR distribution and is likely due to cross-contamination from the other solution.

In all cases, this pruning procedure removes at most 7.5% of the initial 10^4 bootstrap fits before convergence is achieved. With the final pruned distribution, the 90% CL interval is computed as the range between the upper and lower 5% tails.

The 3C parametrization has to be considered with care due to the presence of the two quoted minima (i.e., the 3C-NR and 3C-R). During the bootstrap calculation, cross-contamination between the two solutions is possible, as can be see in, e.g., the histograms in Fig. 7. Similar distribution shapes are also seen in the R_{VMD} values for these cases. Nevertheless, the two solutions can be clearly separated at a 68% CL and the overlap remains relatively mild when considering the 90% CL; thus we expect the uncertainty estimation to be reliable.

[1] S. J. Brodsky, E. Chudakov, P. Hoyer, and J. M. Laget, Phys. Lett. B **498**, 23 (2001).
[2] D. Kharzeev, H. Satz, A. Syamtomov, and G. Zinovjev, Eur. Phys. J. C **9**, 459 (1999).
[3] Y. Guo, X. Ji, and Y. Liu, Phys. Rev. D **103**, 096010 (2021).
[4] K. A. Mamo and I. Zahed, Phys. Rev. D **101**, 086003 (2020).
[5] K. A. Mamo and I. Zahed, Phys. Rev. D **106**, 086004 (2022).
[6] Y. Hatta and D.-L. Yang, Phys. Rev. D **98**, 074003 (2018).
[7] R. Wang, J. Evslin, and X. Chen, Eur. Phys. J. C **80**, 507 (2020).
[8] X. Ji, Front. Phys. (Beijing) **16**, 64601 (2021).
[9] C. Han, W. Kou, R. Wang, and X. Chen, Eur. Phys. J. A **59**, 118 (2023).
[10] R. Wang, W. Kou, Y.-P. Xie, and X. Chen, Phys. Rev. D **103**, L091501 (2021).
[11] D. E. Kharzeev, Phys. Rev. D **104**, 054015 (2021).
[12] K. A. Mamo and I. Zahed, Phys. Rev. D **103**, 094010 (2021).
[13] O. Gryniuk and M. Vanderhaeghen, Phys. Rev. D **94**, 074001 (2016).
[14] I. Strakovsky, D. Epifanov, and L. Pentchev, Phys. Rev. C **101**, 042201 (2020).

[15] L. Pentchev and I. I. Strakovsky, Eur. Phys. J. A **57**, 56 (2021).
[16] X.-Y. Wang, F. Zeng, and I. I. Strakovsky, Phys. Rev. C **106**, 015202 (2022).
[17] M. E. Luke, A. V. Manohar, and M. J. Savage, Phys. Lett. B **288**, 355 (1992).
[18] H. Fujii and D. Kharzeev, Phys. Rev. D **60**, 114039 (1999).
[19] S. J. Brodsky and G. A. Miller, Phys. Lett. B **412**, 125 (1997).
[20] S. J. Brodsky, I. A. Schmidt, and G. F. de Teramond, Phys. Rev. Lett. **64**, 1011 (1990).
[21] J. Tarrús Castellà and G. a. Krein, Phys. Rev. D **98**, 014029 (2018).
[22] T. Barnes, Eur. Phys. J. A **18**, 531 (2003).
[23] R. Rapp and H. van Hees, *Quark-Gluon Plasma 4* (World Scientific, Singapore, 2010), pp. 111–206.
[24] W.-Q. Chao and B. Liu, Gluon shadowing, absorption and charmonium/bottomonium suppression in *hA* processes, Report No. BIHEP-TH-93-12, 1993.
[25] R. Aaij *et al.* (LHCb Collaboration), Phys. Rev. Lett. **115**, 072001 (2015).
[26] R. Aaij *et al.* (LHCb Collaboration), Phys. Rev. Lett. **117**, 082002 (2016).
[27] R. Aaij *et al.* (LHCb Collaboration), Phys. Rev. Lett. **122**, 222001 (2019).
[28] Q. Wang, X.-H. Liu, and Q. Zhao, Phys. Rev. D **92**, 034022 (2015).
[29] V. Kubarovsky and M. B. Voloshin, Phys. Rev. D **92**, 031502 (2015).
[30] M. Karliner and J. L. Rosner, Phys. Lett. B **752**, 329 (2016).
[31] A. N. Hiller Blin, C. Fernández-Ramírez, A. Jackura, V. Mathieu, V. I. Mokeev, A. Pilloni, and A. P. Szczepaniak, Phys. Rev. D **94**, 034002 (2016).
[32] D. Winney, C. Fanelli, A. Pilloni, A. N. Hiller Blin, C. Fernández-Ramírez, M. Albaladejo, V. Mathieu, V. I. Mokeev, and A. P. Szczepaniak (JPAC Collaboration), Phys. Rev. D **100**, 034019 (2019).
[33] E. Y. Paryev, Nucl. Phys. **A1029**, 122562 (2023).
[34] A. Ali *et al.* (GlueX Collaboration), Phys. Rev. Lett. **123**, 072001 (2019).
[35] Z. E. Meziani *et al.*, arXiv:1609.00676.
[36] C. Fanelli, L. Pentchev, and B. Wojtsekhowski, Measurement of the parameters of the LHCb pentaquark states through double polarization asymmetries with SBS in Hall A (2018), https://www.jlab.org/exp-prog/proposals/18/LOI12-18-001.pdf, LoI12-18-001 (PAC 46).
[37] S. Stepanyan *et al.* (CLAS Collaboration), JLab approved experiment E12-12-001A (2017).
[38] S. Joosten and Z. E. Meziani, Proc. Sci. QCDEV2017 (**2018**) 017.
[39] J.-J. Wu, R. Molina, E. Oset, and B. S. Zou, Phys. Rev. Lett. **105**, 232001 (2010).
[40] M.-Z. Liu, Y.-W. Pan, F.-Z. Peng, M. Sánchez Sánchez, L.-S. Geng, A. Hosaka, and M. Pavon Valderrama, Phys. Rev. Lett. **122**, 242001 (2019).
[41] C. Fernández-Ramírez, A. Pilloni, M. Albaladejo, A. Jackura, V. Mathieu, M. Mikhasenko, J. A. Silva-Castro, and A. P. Szczepaniak (JPAC Collaboration), Phys. Rev. Lett. **123**, 092001 (2019).
[42] M.-L. Du, V. Baru, F.-K. Guo, C. Hanhart, U.-G. Meißner, J. A. Oller, and Q. Wang, Phys. Rev. Lett. **124**, 072001 (2020).
[43] M.-L. Du, V. Baru, F.-K. Guo, C. Hanhart, U.-G. Meißner, A. Nefediev, and I. Strakovsky, Eur. Phys. J. C **80**, 1053 (2020).
[44] S. Adhikari *et al.*, Phys. Rev. C **108**, 025201 (2023).
[45] B. Duran *et al.*, Nature (London) **615**, 813 (2023).
[46] D. J. Wilson, J. J. Dudek, R. G. Edwards, and C. E. Thomas, Phys. Rev. D **91**, 054008 (2015).
[47] M. Albaladejo *et al.* (JPAC Collaboration), Prog. Part. Nucl. Phys. **127**, 103981 (2022).
[48] S. Chekanov *et al.* (ZEUS Collaboration), Eur. Phys. J. C **24**, 345 (2002).
[49] A. Aktas *et al.* (H1 Collaboration), Eur. Phys. J. C **46**, 585 (2006).
[50] A. Donnachie and P. V. Landshoff, Phys. Lett. B **437**, 408 (1998).
[51] A. C. Caldwell and M. S. Soares, Nucl. Phys. **A696**, 125 (2001).
[52] U. Camerini, J. G. Learned, R. Prepost, C. M. Spencer, D. E. Wiser, W. Ash, R. L. Anderson, D. Ritson, D. Sherden, and C. K. Sinclair, Phys. Rev. Lett. **35**, 483 (1975).
[53] S. J. Brodsky, P. Hoyer, C. Peterson, and N. Sakai, Phys. Lett. **93B**, 451 (1980).
[54] V. A. Saleev, Mod. Phys. Lett. A **09**, 1083 (1994).
[55] R. D. Ball, A. Candido, J. Cruz-Martinez, S. Forte, T. Giani, F. Hekhorn, K. Kudashkin, G. Magni, and J. Rojo (NNPDF Collaboration), Nature (London) **608**, 483 (2022).
[56] M. Guzzi, T. J. Hobbs, K. Xie, J. Huston, P. Nadolsky, and C. P. Yuan, Phys. Lett. B **843**, 137975 (2023).
[57] W. Kou, R. Wang, and X. Chen, Eur. Phys. J. A **58**, 155 (2022).
[58] X.-Y. Wang, J. Bu, and F. Zeng, Phys. Rev. D **106**, 094029 (2022).
[59] M. Gari and W. Krumpelmann, Phys. Lett. **141B**, 295 (1984).
[60] R. Van Royen and V. F. Weisskopf, Nuovo Cimento A **50**, 617 (1967); **51**, 583(E) (1967).
[61] E. J. Eichten and C. Quigg, Phys. Rev. D **52**, 1726 (1995).
[62] E. Ortiz-Pacheco, R. Bijker, and C. Fernández-Ramírez, J. Phys. G **46**, 065104 (2019).
[63] E. Y. Paryev and Y. T. Kiselev, arXiv:1510.00155.
[64] A. B. Kaidalov and P. E. Volkovitsky, Phys. Rev. Lett. **69**, 3155 (1992).
[65] M. I. Eides, V. Y. Petrov, and M. V. Polyakov, Eur. Phys. J. C **78**, 36 (2018).
[66] A. Sibirtsev and M. B. Voloshin, Phys. Rev. D **71**, 076005 (2005).
[67] G. Krein and T. C. Peixoto, Few-Body Syst. **61**, 49 (2020).
[68] A. Hayashigaki, Prog. Theor. Phys. **101**, 923 (1999).
[69] T. Sugiura, Y. Ikeda, and N. Ishii, J. Phys. Soc. Jpn. Conf. Proc. **26**, 031015 (2019).
[70] K. Yokokawa, S. Sasaki, T. Hatsuda, and A. Hayashigaki, Phys. Rev. D **74**, 034504 (2006).
[71] U. Skerbis and S. Prelovsek, Phys. Rev. D **99**, 094505 (2019).
[72] A. Andronic *et al.*, Eur. Phys. J. C **76**, 107 (2016).
[73] R. Rapp, D. Blaschke, and P. Crochet, Prog. Part. Nucl. Phys. **65**, 209 (2010).

[74] M. B. Voloshin, Prog. Part. Nucl. Phys. **61**, 455 (2008).
[75] J. P. Hilbert, N. Black, T. Barnes, and E. S. Swanson, Phys. Rev. C **75**, 064907 (2007).
[76] R. L. Anderson *et al.*, Phys. Rev. Lett. **38**, 263 (1977).
[77] J. Hufner and B. Z. Kopeliovich, Phys. Lett. B **426**, 154 (1998).
[78] D. Kharzeev and H. Satz, Phys. Lett. B **334**, 155 (1994).
[79] N. F. Black, KN and $J/\psi N$ scattering in the quark model, Ph.D. thesis, Tennessee U., 2002.
[80] K. Martins, Prog. Part. Nucl. Phys. **36**, 409 (1996).
[81] Y.-s. Oh, T. Song, and S. H. Lee, Phys. Rev. C **63**, 034901 (2001).
[82] W. Liu, C. M. Ko, and Z. W. Lin, Phys. Rev. C **65**, 015203 (2002).
[83] R. Molina, C. W. Xiao, and E. Oset, Phys. Rev. C **86**, 014604 (2012).
[84] A. M. Badalian, L. P. Kok, M. I. Polikarpov, and Y. A. Simonov, Phys. Rep. **82**, 31 (1982).
[85] I. Strakovsky, W. J. Briscoe, E. Chudakov, I. Larin, L. Pentchev, A. Schmidt, and R. L. Workman, Phys. Rev. C **108**, 015202 (2023).
[86] P. Bosted, C. Chudakov *et al.*, The A-dependence of J/ψ photoproduction near threshold (2007), https://www.jlab.org/exp-prog/proposals/07/PR12-07-106.pdf PR12-07-106 (PAC 32).
[87] J. Arrington *et al.* (Jefferson Lab SoLID Collaboration), arXiv:2209.13357.
[88] R. Abdul Khalek *et al.*, Nucl. Phys. **A1026**, 122447 (2022).
[89] D. P. Anderle *et al.*, Front. Phys. (Beijing) **16**, 64701 (2021).
[90] J. Arrington *et al.*, Prog. Part. Nucl. Phys. **127**, 103985 (2022).
[91] A. Accardi *et al.*, arXiv:2306.09360.
[92] D. Winney, A. Pilloni, V. Mathieu, A. N. Hiller Blin, M. Albaladejo, W. A. Smith, and A. Szczepaniak (JPAC Collaboration), Phys. Rev. D **106**, 094009 (2022).
[93] M. Albaladejo, A. N. Hiller Blin, A. Pilloni, D. Winney, C. Fernández-Ramírez, V. Mathieu, and A. Szczepaniak (JPAC Collaboration), Phys. Rev. D **102**, 114010 (2020).
[94] JPAC Collaboration, Code for Dynamics in near-threshold J/ψ photoproduction (2023), 10.5281/zenodo.8302620.